Revision 2

Word count: 7092

High - pressure polymorphs of the ferroan dolomite: possible host structures for carbon in the lower mantle

Naira S. Martirosyan[1,2,3*], Ilias Efthimiopoulos[1#], Sandro Jahn[2], Sergey S. Lobanov[1], Richard Wirth[1], Hans-Josef Reichmann[1], Monika Koch-Müller[1]

[1] GFZ German Research Centre for Geosciences, Telegrafenberg, 14473 Potsdam, Germany

[2] Institute of Geology and Mineralogy, University of Cologne, Zülpicher Str. 49b, 50674 Köln, Germany

[3] Bayerisches Geoinstitut, University of Bayreuth, Universitätsstraße 30, 95447 Bayreuth, Germany

#Present address: Max-Planck-Institut für Eisenforschung GmbH, Max-Planck-Str. 1, 40237 Düsseldorf

*Corresponding author: naira.martirosyan@uni-bayreuth.de

Abstract

In this study, we investigated four different ferroan dolomite samples using in situ Raman spectroscopy and powder X-ray diffraction (XRD) at high pressures up to 48 GPa and at room temperature. Our results show that the transition from Dolomite-I (Dol-I) to Dolomite-II (Dol-II) occurs above 13-16 GPa, and the transition pressure depends on the composition of the solid solution. Compression above 32-35 GPa results in the appearance of the Dolomite-IIIc (Dol-IIIc) or Dolomite-IIIb (Dol-IIIb). In the high-pressure XRD study, we found that the XRD patterns of the $Ca_{0.97}(Mg_{0.77},Fe_{0.23}Mn_{0.03})(CO_3)_2$ (*xFe* = 0.23, Ank23) can be indexed as Dol-IIIc at 44 GPa, while the rhombohedral Dol-IIIb structure matches better with the XRD patterns of the *xFe* = 0.40 (Ank40) and 0.64 (Ank64) solid solutions. Additionally, in the Raman spectra of the Fe-richest sample (Ank64), we observed an abrupt frequency downshift of the CO_3-stretching vibrations between 40 – 42 GPa, which may reflect a pressure-induced Fe^{2+} spin transition.

We further investigated two samples with *xFe*= 0.19 (Ank19) and 0.23 (Ank23) at high-pressure and high temperatures, up to at least 2600 K. The experiments revealed that the unquenchable Dol-IIIc structure could be a stable high-pressure/high-temperature polymorph in ferroan dolomite up to at least 2600 K.

Key words: deep carbon cycle, dolomite, solid solution, phase diagram, phase transition, high pressure, Raman spectroscopy

1. Introduction

A large amount of carbon is stored in the Earth's interior and constitutes the deep carbon cycle driven by plate tectonics (Sleep and Zahnle, 2001; Plank and Manning, 2019). Carbonates, predominantly calcite and dolomite, occurring in marine sediments, hydrothermally altered basalts, and carbonated serpentinites are the major carbon-bearing minerals of the oceanic crust (Plank and Manning, 2019). Depending on the pressure–temperature–time path experienced by each subduction slab and the amount of aqueous fluid present, about 20–80% of Ca, Mg, Fe- carbonates could remain after decarbonation and melting beneath island arcs and be further transported beyond ~150 km depth to the deep mantle (Kelemen and Manning, 2015; Plank and Manning, 2019). The primary inclusions in superdeep diamonds contain dolomite and Ca-carbonate, which confirm their existence in the deep mantle (Stachel et al., 1998, 2000; Walter et al., 2008; Wirth et al., 2009). The identification and characterization of the high–pressure behavior of carbonates is an important step towards the understanding of the deep carbon cycle and the role of carbon-bearing phases in mantle processes. While it is well established that Mg- and Ca-carbonate have stable polymorphs at mantle conditions (Boulard et al., 2011; Lobanov et al., 2017), the high-pressure behavior of dolomite is still not well understood.

Dolomite ($CaMg(CO_3)_2$), forms solid solutions with ankerite ($CaFe(CO_3)_2$) with Fe^{2+} substituting up to 70% of Mg^{2+} in natural samples (Reeder and Dollase, 1989). According to the nomenclature proposed by Reeder (1983), solid solutions with Fe<Mg are named ferroan dolomite, while Fe>Mg – ankerite. At ambient conditions dolomite, ferroan dolomite, and ankerite adopt a trigonal structure (Dol-I, space group (SG) *R*-3) with nearly planar triangular CO_3 units and alternating layers of CaO_6 and $(Mg,Fe)O_6$ octahedra (Reeder and Dollase, 1989).

Room temperature experiments show that dolomite-ankerite solid solutions have two high-pressure polymorphs (Mao et al., 2011; Merlini et al., 2012, 2017). Pressure increase to 15–20 GPa leads to the phase transition from Dol-I to Dol-II (Mao et al., 2011; Merlini et al., 2012; Efthimiopoulos et al., 2017, 2019; Binck et al., 2020; Vennari and Williams, 2018; Zhao et al., 2020; Chuliá-Jordán et al., 2021). A single-crystal X-ray diffraction study reported a triclinic structure (SG *P*-1) for Dol-II with tilted CO_3 groups and eightfold coordination of the Ca and Mg/Fe cations with respect to the oxygen anions (Merlini et al., 2012) (Fig. S1).

Further increase of pressure above 35 GPa results in the formation of a second high-pressure polymorph named Dolomite-III (Dol-III) (Mao et al., 2011; Merlini et al., 2012).

The structure of Dol-III was first reported by Mao et al. (2011) who conducted powder X-ray diffraction (XRD) experiments on Fe-poor dolomite (*xFe* = 0.078). The XRD patterns were attributed to a phase with monoclinic symmetry, yet no more structural details were provided. Later, the single-crystal studies by Merlini et al. (2012, 2017) and Binck et al. (2020) showed that the behavior of the dolomite-ankerite solid solution above 35 GPa is more complex than originally thought, as three different candidate structures have been proposed: Dol-III, Dol-IIIb and Dol-IIIc (Fig. S1).

In pure dolomite, the high-pressure polymorph crystallizes in a triclinic space group (SG *P*-1, Dol-IIIc) (Binck et al., 2020), while two different structures have been proposed for ferroan dolomite (*xFe* = 0.40): a rhombohedral (SG *R*3, Dol-IIIb) (Merlini et al., 2017) and a triclinic phase (SG *P*-1, Dol-III) (Merlini et al., 2012). All three phases are topologically similar and very close to each other from a structural point of view. The main difference between Fe-poor (Dol-IIIc) and Fe-rich phases (Dol-III or IIIb) is the degree of tilting of the CO_3 groups (Binck et al., 2020). The different symmetries show that the stability and transformation path of the Dol-III, IIIb, IIIc polymorphs can be strongly affected by variations in Fe-content and experimental conditions. What structures are adopted by other members of the dolomite-ankerite solid solution is currently unknown. The abbreviation Dol-III/IIIc/IIIb will be used to refer further to the high-pressure phases of dolomite-ankerite solid solutions adopted above 35 GPa with currently unknown structures.

As high-pressure polymorphs of dolomite and ferroan dolomite could represent a reservoir for carbon storage within the deep mantle, it is important to study the high-temperature behavior of the dolomite-ankerite solid solutions. Pure end-member $CaMg(CO_3)_2$ undergoes a breakdown reaction to magnesite and Ca-carbonate above 5 GPa at high temperatures (Shirasaka et al., 2002; Merlini et al., 2012). Starting from about 8 GPa the reaction curve is above the hot subduction geotherm (Shirasaka et al., 2002). However, high-pressure polymorphs of ferroan dolomite ($xFe = 0.40$) may be resistant to decomposition into single-cation carbonates as shown by Merlini et al. (2012).

The complex behavior of the high-pressure polymorphs and the possible stability of ferroan dolomite at high temperatures and pressures should be addressed experimentally. Here, the structural changes of the dolomite-ankerite solid solutions as a function of composition were studied by Raman spectroscopy and powder X-ray diffraction up to 48 GPa at room temperature (Fig. 1) and at 38-43 GPa and high temperature.

2. Methods

2.1. Synthesis and sample characterization

Four samples from the dolomite-ankerite solid solution series with different Fe contents (Table 1) were studied in the high-pressure experiments. In this paper, we used the abbreviation Ank19, Ank23, Ank40, Ank64 to refer to the samples with different Fe content as it helps to differentiate the sample names from the names of the different high-pressure polymorphs (Dol-I, Dol-II, Dol-III/IIIc/IIIb).

The first sample, Ank19, was synthesized using a piston-cylinder high-pressure apparatus at GFZ, Potsdam. Synthetic powders of $CaCO_3$ (99.0% purity, Merck Millipore Corporation), $FeCO_3$ (see Cerantola et al. (2015) for details), and natural magnesite ($Mg_{0.985}Fe_{0.008}Mn_{0.004}Ca_{0.003}CO_3$ (Bahia, Brazil)) were used as starting materials for synthesis. The starting powder was prepared with a stoichiometry of $Ca(Mg_{0.8}Fe_{0.2})(CO_3)_2$. We used a double capsule technique with Au as capsule material. Carbonate mixture was packed into the inner capsule, which was further placed within an outer capsule along with approximately 100 mg of $Ag_2C_2O_4$ as the buffer material. Both ends of the outer capsule were sealed by arc welding. The experiment was conducted at 1.8 GPa, 850°C for 26 h. The synthesis resulted in the formation of a homogeneous $Ca(Mg_{0.81}Fe_{0.19})(CO_3)_2$ solid solution (Table 1).

Three remaining samples were natural ferroan dolomites and ankerite from (i) Salzburg, Austria (Ank23, $Ca_{0.97}(Mg_{0.77},Fe_{0.23}Mn_{0.03})(CO_3)_2$), (ii) Thüringer Wald, Germany (Ank40, $Ca(Mg_{0.56},Fe_{0.40}Mn_{0.06})(CO_3)_2$) and (iii) Steiermark, Austria (Ank64, $Ca(Mg_{0.33},Fe_{0.64}Mn_{0.05})(CO_3)_2$) (Table 1).

The selected samples were mounted in epoxy, polished and carbon-coated. The chemical composition and homogeneity of the samples were characterized by electron microprobe analysis using JEOL Hyperprobe JXA-8500F EMP with a field emission cathode (GFZ, Potsdam). Analyzes were conducted at a 15 kV acceleration voltage, a 10 nA beam current, and a 0.5-10 μm beam size. Dolomite, calcite, and siderite with known compositions were used as standard materials (Table 1). In addition to that, the structural analysis was performed at ambient conditions with powder X-ray diffraction (XRD) to confirm the initial Dol-I structure. The XRD patterns were collected using STOE Stadi P diffractometer equipped with a curved Germanium (111) primary monochromator, a high-resolution MYTHEN-detector and a normal focus Cu X-ray tube (Cu-$K_{\alpha1}$ radiation) (GFZ, Potsdam). The XRD data were processed with the GSAS software package combined with the graphical interface EXPGUI (Larson and Von Dreele, 1994; Toby, 2001). Unit cell parameters were obtained by Pawley refinements (Table S1). The structural parameters for dolomite and ferroan dolomite determined by Reeder and Dollase (1989) were used as a starting model.

2.2. Preparation of the high-pressure experiments

Experiments were performed with a symmetric piston-cylinder diamond anvil cell (DAC) equipped with diamonds with 300 μm culet size. Rhenium gaskets were indented to 30-40 μm and drilled in the center of the indentation to form a sample chamber with a diameter of 140 μm. Either selected crystals (for Raman spectroscopy experiments) or fine powder (for XRD measurements) were placed into the sample chamber together with a ruby pressure sensor. Before and after each Raman and XRD measurement, the pressure was determined based on the spectral position of the ruby (Al_2O_3:Cr^{3+}) fluorescence line with an accuracy of 2-5 % up to 55 GPa (Shen et al., 2020).

The previous studies showed a clear dependence of the high-pressure behavior of pure dolomite on hydrostatic conditions (Efthimiopoulos et al., 2019). To test the effect of hydrostaticity on the phase transformations of dolomite-ankerite solid solutions, three different pressure media (PM), i.e. NaCl, Ar, and Ne with different hydrostatic ranges (Klotz et al. 2009), were used in the high-pressure Raman experiments on the Ank19 sample (Fig. 1, S2-S5). Three experiments with Ar and NaCl were conducted up to 33 GPa (Fig. 1). At these conditions non-hydrostaticity caused the disappearance of the Raman signal below 1000 cm^{-1} (Fig. S2, S3). In all other Raman and XRD experiments, Ne was used as a PM, which allowed the acquisition of reliable data up to at least 48 GPa (Fig. 1).

2.3. High-pressure experiments at room temperature

The vibrational properties of dolomite-ankerite solid solutions were studied *in situ* using Raman-spectroscopy. Measurements were performed with a HORIBA Jobin Yvon LabRAM HR800 UV-VIS spectrometer (GFZ, Potsdam) equipped with a blue (λ = 473 nm) diode-pumped solid-state laser. The grating had 1800 lines/mm, the slit aperture was set to 500 μm, and the confocal pinhole had a diameter of 50 μm. The Raman spectra were obtained in the spectral range of 140-1250 cm^{-1} with an acquisition time of 120 s and 5 accumulations. Three independent runs for each sample were performed. The spectra were collected at ambient conditions before and after the experiments and at high pressures upon compression in 1-2 GPa step (Fig. 1). The software Fityk was used for data analysis (Wojdyr, 2010).

The diffraction experiments were carried out up to 44 GPa using a focused monochromatic beam ($\lambda = 0.2906$ Å) at the extreme condition beamline P02.2 at Petra-III (DESY, Hamburg, Germany) (Liermann et al., 2015). XRD patterns were acquired every 1-2 GPa at ambient temperature using a Perkin Elmer XRD 1621 flat-panel detector (Fig. 1). The exposure time was typically 15-20 s. In order to improve powder averaging, the DAC was continuously rocked by ±7° during measurement. The diffraction images were integrated using the Dioptas software (Prescher and Prakapenka, 2015). The lattice parameters and unit cell volumes were obtained with GSAS software (Table 2).

2.4. High-temperature stability of the high-pressure dolomite polymorphs above 38 GPa

High-temperature experiments were performed in the range of 38-43 GPa on two samples: Ank19 and Ank23. Once at the target pressure, the samples were heated using laser-heating technique by a continuous-wave 100 W, 1070 nm, YLR-100-AC (IPG Photonics) Yb fiber laser with a nearly flat-top intensity distribution and beam size of ∼10 µm in the focal plane (Lobanov et al., 2020). The temperature was estimated by fitting thermal emission spectra to a grey-body Planck radiation function with T-Rax software (developed by C. Prescher).

Raman spectroscopy measurements were performed before and after the heating, and at ambient conditions on the recovered samples. Additionally, the samples were analyzed using transmission electron microscopy (TEM) for microtextural observation, and structural and chemical analysis. Thin sections of approximately $15 \times 10 \times 0.15\ \mu m^3$ in size were prepared with a focused Ga-ion beam (FIB) system (FEI FIB 200 TEM) (Wirth, 2009) perpendicular to the laser-heated spot, and analyzed in FEI Tecnai G2 F20 X-Twin transmission electron microscope (GFZ, Potsdam).

3. Results and discussion

3.1. High-pressure phase transitions of dolomite-ankerite solid solutions

The results of the in situ Raman study are summarized in Figures 2 – 6. At ambient conditions, 8 Raman (R) and 10 infrared (IR) vibrational modes are expected for Dol-I at the center of the Brillouin zone Γ given by group theory (Yamamoto et al. 1975). The Raman spectra of the dolomite-ankerite solid solutions collected at ambient conditions display four high-intensity modes (Fig. 2). The high-frequency modes (700-1300 cm^{-1}) are attributed to the internal vibrations of the CO_3 groups: symmetric stretching (ν_1 ~1100 cm^{-1}) and in-plane bending (ν_4 ~730 cm^{-1}). The low-frequency modes correspond to the lattice vibrations which are defined by the motions of the CO_3 groups against the cations (Rividi et al., 2010).

The Raman-active modes of Fe-free dolomite with Dol-I structure are located at 176, 298, 725, and 1097 cm^{-1} (Rividi et al., 2010) and shift to lower wavenumbers with increasing Fe-concentration (Fig. 2). The observed shift is consistent with previous studies and is due to the substitution of Mg^{2+} by the larger and heavier Fe^{2+} (Rividi et al., 2010). The positions of the high-frequency modes ν_1 and ν_4 show marginal dependence on the Fe content and shift by a total of 5 cm^{-1} (ν_4) and 8 cm^{-1}(ν_1) in the solid solutions with xFe = 0 - 0.64 (Fig. 2). Since both modes correspond to internal CO_3 vibrations and thus, poorly involve the Fe–Mg cations (White, 1974), such small effect of composition on the Raman mode frequencies is expected. Raman modes associated with the lattice vibrations, on the other hand, defined by the relative motions of the molecular unit CO_3 groups against the cations (White, 1974), show significantly larger frequency variations with Fe composition: from 176 to 161 cm^{-1} (T), and from 298 to 276 cm^{-1} (L) for xFe = 0-0.64.

According to the vibrational studies on dolomite samples (x<0.02) (Efthimiopoulos et al., 2017; Efthimiopoulos et al., 2019; Binck et al., 2020), the characteristic Dol-I lattice vibration mode (176 cm^{-1}) shows a splitting above 9 GPa. A splitting of the low-frequency mode around 201 cm^{-1} was also reported by Zhao et al. (2020) at 7.8 GPa for ferroan dolomite (xFe = 0.2). It was interpreted as a local structural distortion of Dol-I and the corresponding phase was labeled Dol-Ib (Efthimiopoulos et al., 2017; Binck et al., 2020). Dol-Ib was only observed in the spectroscopic studies in the pressure range of 8-16 GPa.

In the present experiments, no clear splitting of the lattice mode could be observed in any of the studied samples (Fig. 3, S2-S6). The appearance of a shoulder on the high-frequency side of the 195 cm^{-1} (at 205 cm^{-1}) above 9 GPa was detected in Ank19, when Ar and NaCl pressure media were used (Fig. S2 – S4). However, this splitting is not observed in experiments conducted with Ne PM with Ank23, Ank40 or Ank64 (Fig. 3, S5, S6). It is likely that the local structural distortion of the Dol-I phase can be caused by a non-hydrostatic environment and will not take place in the ferroan dolomite or ankerite at quasi-hydrostatic conditions.

The Raman spectra of all studied dolomite-ankerite solid solutions collected up to 13.7-16 GPa (depending on the composition) can be characterized by the same set of modes for the Dol-I phase (Fig. 3, S5, S6). Further increase of pressure leads to the phase transition to Dol-II. According to the group theory, a total sum of 27 IR and 30 Raman active modes are expected for the Dol-II phase (Efthimiopoulos et al. 2017). The appearance of Dol -II is marked by new features in the Raman spectra below 600 cm^{-1} and the broadening of the v_1 mode (Figs. 3, S4-S8). The transition pressure from Dol-I to Dol-II depends on the composition of the solid solution and has a negative linear correlation with Fe content: Dol-II forms at ~16 GPa in Ank19 and at 13.7 GPa in Ank64 (Fig. 1).

Above 32 – 35 GPa the Dol-III/IIIc/IIIb modification is adopted (Fig. 4 - 6). The transition pressure increases slightly with the Fe-content (Fig. 1). High-pressure phase appears at 35 GPa in Ank19 (Fig. S5), and at 37.3 GPa in Ank64 (Fig. 5). The observed correlation is consistent with the high-pressure Raman and XRD studies of ferroan dolomites

(Merlini et al., 2012; Merlini et al., 2017; Zhao et al., 2020; Chuliá-Jordán et al., 2021). However, there is a clear discrepancy with the studies on the Fe-poor solid solutions ($xFe < 0.08$). The Dol-II to Dol-IIIc transition in the Fe-poor dolomite was observed at 40-41 GPa (Mao et al., 2011; Vennari and Williams, 2018; Efthimiopoulos et al., 2019; Binck et al., 2020), showing an abrupt drop in the transition pressure by 5-6 GPa between solid solutions with $xFe = 0.08$ and 0.19.

The Raman spectra of the Dol-III/IIIc/IIIb phases are characterized by the appearance of the new low-frequency vibrational modes below 800 cm^{-1} (Fig. 4, 5, S7), due to a broad suite of divalent cation environments and a plethora of possible divalent cation/CO_3 vibrational interactions within the high-pressure structure (Merlini et al., 2012, 2017). Inspection of the CO_3 stretching vibration frequency region at 1100-1200 cm^{-1} reveals the presence of at least 5-6 Raman components, as opposed to the three components of the Dol-II structure (Fig. 6, S8).

To show how the CO_3 stretching vibrations change with the composition of the solid solution, Raman spectra in the 900-1270 cm^{-1} frequency range collected at similar experimental conditions (~40 GPa, Ne PM) are plotted in Fig. 6. According to the previous studies, the symmetric stretching vibrations in Fe-poor Dol-IIIc are represented by at least six Raman components (Fig. 6e) (Efthimiopoulos et al., 2019). The highest intensity feature is located at 1210 cm^{-1} with three clear sidebands (1170 cm^{-1}, 1190 cm^{-1}, and 1230 cm^{-1}) (Fig. 6e) (Efthimiopoulos et al., 2019). With increasing Fe content, the Raman bands merge initially into a broad multiplet feature, whereas a successive frequency downshift and intensity enhancement of the lower-frequency bands at the expense of the higher-frequency components takes place (Fig. 6). Such behavior can be rationalized by the decrease of C-O bond force constant (frequency downshift of stretching vibrations) and the electronic polarizability change associated with the stretching vibrations (intensity variations) upon increasing the Fe concentration in the Dol-III/IIIc/IIIb phase.

Finally, in the case of the Ank64 sample, an abrupt frequency downshift of the Raman-active stretching vibrations was observed between 40-42 GPa (Fig. 5). Considering the similar behavior in the Raman spectra of the siderite and the magnesite-siderite solid solution series in the vicinity of the Fe spin transition (e.g., Müller et al. 2017), this effect is most likely stemming from the pressure-induced Fe^{2+} spin transition in the Ank64 sample. Notably, the apparent iron spin transition takes place after the high-pressure phase is adopted in Ank64, and the spin transition pressure lies ~5 GPa lower compared to the magnesite-siderite solid solution series transition (e.g., Müller et al. 2017).

3.2. High-pressure XRD measurements

We have additionally conducted a high-pressure XRD study on the Ank40, Ank23, and Ank64 samples at ambient temperature. The results are plotted in Fig. 7, S9-S13, and Table 2. In this pressure range, the ferroan dolomite undergoes two well-defined phase transitions to Dol-II and to high-pressure Dol-IIIc or IIIb (Fig. S9-S12). The first phase transition was detected at 1-2 GPa higher pressures compared to the Raman data. The XRD measurements confirm a dependence of the Dol-I to Dol-II transition on the chemical composition and decrease of the transition pressure with increasing Fe content.

The high-pressure phase transition to Dol-IIIb or IIIc polymorphs was detected at 34-35 GPa, which is in good agreement with the Raman data. For the Ank23 sample, the Dol-IIIc phase can readily index the powder XRD pattern at 44 GPa, whereas the rhombohedral Dol-IIIb structure matches better the XRD pattern of Ank40 at 41 GPa (Table 2, Fig. 7, S13). The main difference in the XRD patterns of the two phases can be observed in the 6-8° 2θ diffraction angle region. Dol-IIIc phase exhibits at least five clear Bragg features, while the

Dol-IIIb polymorph shows two asymmetric Bragg features. Nevertheless, both the Ank23 and Ank40 XRD patterns show distinct similarities above 8°, pointing to the structural affinity of the Dol-IIIc and Dol-IIIb modifications. We should remind here that the main structural difference between the Dol-IIIc and Dol-IIIb polymorphs is the tilting of the CO_3 units, with the Dol-IIIb phase exhibiting a higher tilting degree (Binck et al., 2020; Merlini et al., 2012; Merlini et al., 2017).

As for the Ank64 sample at 38 GPa, a clear distinction between the Dol-IIIc and Dol-IIIb polymorphs is not that straightforward, as its XRD pattern contains also traces of the remnant Dol-II phase. Given that the Dol-IIIc phase appears to be adopted for samples without iron or with low Fe content (Binck et al., 2020; Merlini et al., 2012; Merlini et al., 2017), we have tentatively indexed the Ank64 pattern with the Dol-IIIb polymorph (Fig. S14). However, further study could be beneficial to determine the structure that Ank64 adopts.

The corresponding structural parameters are listed in Table 2. Interestingly, we note that both the Ank40 and Ank64 samples exhibit lower volumes (at lower pressures) compared to the Ank23 sample; these lower values may be connected to a pressure-induced Fe^{2+} spin transition effect ‘kicking in’ for higher Fe contents, consistent with the observed changes in the Fe-rich Ank64 Raman spectra (Fig. 5).

3.3. High-temperature behavior of Dol-IIIc

To investigate the stability of Dol-IIIc at the Earth’s lower mantle conditions, two samples Ank19 and Ank23 were studied after heating. First, the pressure was increased to 38-43 GPa at room temperature to transform the starting material into Dol-IIIc, and then the samples were heated up to 2600 K.

No changes were observed in the high-pressure Raman spectra after annealing up to 2600 K (Fig. S15). The Raman spectra collected after the temperature quench correspond to the initial phase. The samples recovered at ambient conditions had transformed back into the original Dol-I structure, and no breakdown reaction products were detected. Thus, the present observations reveal that the unquenchable Dol-IIIc structure is stable after heating up to at least 2600 K.

Further attempts to heat Ank23 above 2600 K at 43 GPa failed, as a small increase in laser power produced a runaway of the temperature (flash heating event). The observed plateau at 2600 K indicates a decrease in the laser absorption and could be considered as circumstantial evidence for the melting of the laser absorber (Geballe and Jeanloz, 2012) i.e. Ank23. A melting process at the same conditions was reported by Merlini et al. (2012) in the X-ray diffraction study of ferroan dolomite with $xFe = 0.40$.

Raman spectra of Ank23 collected after temperature quench in the experiment with the flash heating event show a broadening of the modes at around 1200 cm^{-1}. Due to the broad features and low quality of the spectra, it cannot be unequivocally decided whether phase transitions or decomposition processes happened. However, after pressure quench, the bands in the Raman spectra of the heated area could be assigned to a mixture of phases (Fig. 8). The most intense feature is a band at 1086 cm^{-1}, which corresponds to calcite (Fig. 8a). The low-frequency vibrations could be defined by two components: the main bands at 150 and 260 cm^{-1} each with a shoulder on the high-frequency side (Fig. 8a). The low-frequency features could hint on the presence of two carbonates: calcite, which is predominant in the Raman spectra, and the ferroan dolomite. The remaining bands at 445, 540, 660 cm^{-1} cannot be explained by any carbonates (Fig. 8a). Those bands could be caused by the presence of Fe,Mg – oxides (hematite, magnetite, or $Fe_{1-x}O$ wüstite). Hematite (Fe_2O_3) is associated with bands near 530 and 440–450 cm^{-1} (Chamritski and Burns, 2005). The Raman spectrum of magnetite (Fe_3O_4) has characteristic modes at 540 cm^{-1} and 666 cm^{-1} (Chamritski and Burns, 2005). Wüstite (FeO) is cubic and should not be visible in Raman spectra. However, a previous study observed a band at 670 cm^{-1} related to the presence of vacancies in the wüstite microstructure (wüstite $Fe_{1-x}O$) (Ovsyannikov et al., 2010).

The perpendicular cross-section of the laser-heated spot in the Ank23 sample was analyzed with TEM to obtain information on the textures, spatial relationships, and semi-quantitative chemical compositions of the solid phases. The obtained TEM images (Fig. 8b,c) confirm a multiphase assemblage in the heated spot and show a zonation of the sample. The zonation appears to be associated with the temperature gradient as phase assemblages change with the distance from the center of the laser beam. The "hot area" consists of amorphous Ca,Mg,Fe-carbonate, which likely represents a quenched dolomitic melt (Fig. 8b). Large round bubbles are observed together with the amorphous ferroan dolomite, indicating the exsolution of fluid from the melt. At the far end of the sample, a layer of calcite is detected (Fig. 8b). The observed phase relations both in Raman and TEM analyses reflect an incongruent melting in the studied Ank23 at 43 GPa above 2600 K. As a flash happened during the laser heating, the exact temperature of the process cannot be determined.

Considering the results of the present study and high-temperature observations of Merlini et al. (2012), it is evident that Dol-IIIc and IIIb are stable phases in the ferroan dolomite above ~35-37 GPa up to 2600 K. On the contrary, Binck et al. (2020) showed decomposition of the Fe-poor Dol-IIIc at 39.5 GPa and 1800-2300 K with a formation of magnesite, postaragonite and dolomite-V. Dolomite-V is a high-temperature, high-pressure polymorph reported only in the Fe-poor system (Binck et al., 2020). It was not observed in ferroan dolomite (Merlini et al. 2012). It appears that the introduction of Fe to dolomite stabilizes the high-pressure Dol-IIIc or IIIb phase over the decomposition reaction product.

4. Implications

The results of the present study show a complex polymorphism of the dolomite-ankerite solid solutions at high pressure and a clear effect of cationic substitution on the phase behavior. The first phase transition from Dol-I to Dol-II exhibits a negative linear correlation with iron content. Depending on the Fe-content, the Dol-III/IIIb polymorphs adopted at higher pressure above 35-40 GPa have different crystal structures: Fe poor solid solutions adopt the triclinic Dol-IIIc phase ($xFe < 0.23$), whereas the rhombohedral Dol-IIIb structure appears for iron-rich samples (at $xFe = 0.40, 0.64$).

High-temperature experiments also show drastic differences in the stability of the dolomite and the ferroan dolomite with respect to decomposition. Fe - poor dolomite undergoes a breakdown reaction to magnesite and Ca-carbonate above 5 GPa at moderate temperature (Shirasaka et al., 2002). Thermodynamic calculations indicate that all the high-pressure dolomite phases are metastable with respect to magnesite and aragonite (Efthimiopoulos et al., 2017). Indeed, previous experimental studies (Binck et al. 2020) demonstrated formation of the dolomite-V + magnesite + post-aragonite assembly at 39.5 GPa and 1880 K.

This scenario, however, changes drastically in the dolomite-ankerite solid solutions. While in the field of Dol-II crystallization, decomposition happens at 2,000–2,400 K regardless of the composition (Merlini et al., 2012), above 35 GPa the Dol-IIIc and IIIb phases persist at high temperatures in the $xFe > 0.19$ mol% solid solutions. It was demonstrated in the present study (in the solid solutions with $xFe = 0.19$ and 0.23) and by Merlini et al (2019) ($xFe = 0.40$) that the Dol-IIIc and IIIb could be indeed stable high-pressure, high-temperature polymorphs in the Fe-containing systems.

The present study reflects that with the stabilization of Dol-IIIc and Dol-IIIb phases, carbonates in the dolomite-ankerite solid solution series may constitute fundamental accessory phases in the lower mantle and represent a possible carrier of carbon in the subduction zones. Given the significant role of carbonates in the petrological and geochemical processes, such as carbonatitic melt formation, metasomatism, and red-ox reactions, the Dol-IIIc and IIIb polymorphs should be considered in the modeling of the lower mantle processes related to the deep carbon cycle.

Acknowledgements

We thank Lea Pennacchioni for her contribution to the paper. This study was partly supported by Deutsche Forschungsgemeinschaft within the Research Unit FOR2125 under grant KO1260/16, JA1469/9, EF112/1, WI1232, and SP1216/7-1. S.S.L. acknowledges the support of the Helmholtz Young Investigators Group CLEAR (VH-NG-1325). We acknowledge DESY (Hamburg, Germany), a member of the Helmholtz Association HGF, for the provision of experimental facilities. Parts of this research was carried out at the Petra-III, P02.2 beamline. We thank Sergey Rashchenko (Sobolev Institute of Geology and Mineralogy, Russia) and Hans-Peter Nabein (GFZ) for their assistance with XRD measurements. We are thankful to the Natural History Museum of Berlin for providing us with samples: Ank40 (sample 2008-15895), Ank23 (sample 1998-2093) and Ank64 (sample 1998-2098).

References

Binck, J., Chariton, S., Stekiel, M., Bayarjargal, L., Morgenroth, W., Milman, V., Dubrovinsky, L., and Winkler, B. (2020). High-pressure, high-temperature phase stability of iron-poor dolomite and the structures of dolomite-IIIc and dolomite-V. Physics of the Earth and Planetary Interiors, 299, 106403.

Boulard, E., Gloter, A., Corgne, A., Antonangeli, D., Auzende, A.L., Perrillat, J.P., Guyot, F., and Fiquet, G. (2011). New host for carbon in the deep Earth. The Proceedings of the National Academy of Sciences USA, 108, 5184-7.

Cerantola, V., McCammon, C., Kupenko, I., Kantor, I., Marini, C., Wilke, M., Ismailova, L., Solopova, N., Chumakov, A., and Pascarelli, S. (2015). High-pressure spectroscopic study of siderite ($FeCO_3$) with a focus on spin crossover. American Mineralogist, 100, 2670-2681.

Chamritski, I., and Burns, G. (2005). Infrared-and Raman-active phonons of magnetite, maghemite, and hematite: a computer simulation and spectroscopic study. The Journal of Physical Chemistry B, 109, 4965-4968.

Chuliá-Jordán, R., Santamaria-Perez, D., Ruiz-Fuertes, J., Otero-de-la-Roza, A., and Popescu, C. (2021). Compressibility and Phase Stability of Iron-Rich Ankerite. Minerals, 11, 607.

Clift, P.D., 2017. A revised budget for Cenozoic sedimentary carbon subduction. Reviews of Geophysics, 55, 97-125.

Efthimiopoulos, I., Germer, M., Jahn, S., Harms, M., Reichmann, H.J., Speziale, S., Schade, U., Sieber, M., and Koch-Müller, M. (2019). Effects of hydrostaticity on the structural stability of carbonates at lower mantle pressures: the case study of dolomite. High Pressure Research, 39, 36-49.

Efthimiopoulos, I., Jahn, S., Kuras, A., Schade, U., and Koch-Müller, M. (2017). Combined high-pressure and high-temperature vibrational studies of dolomite: phase diagram and evidence of a new distorted modification. Physics and Chemistry of Minerals, 44, 465-476.

Geballe, Z.M., and Jeanloz, R. (2012). Origin of temperature plateaus in laser-heated diamond anvil cell experiments. Journal of applied physics, 111, 123518.

Kelemen, P.B., and Manning, C.E. (2015). Reevaluating carbon fluxes in subduction zones, what goes down, mostly comes up. Proceedings of the National Academy of Sciences, 112, E3997-E4006.

Klotz, S., Chervin, J.C, Munsch, P., and Le Marchand, G. (2009). Hydrostatic limits of 11 pressure transmitting media. Journal of Physics D: Applied Physics 42(7), 075413.

Larson, A.C., and Von Dreele, R.B. (1994). GSAS. General Structure Analysis System. LANSCE, MS-H805, Los Alamos, New Mexico.

Liermann, H.P., Konôpková, Z., Morgenroth, W., Glazyrin, K., Bednarčik, J., McBride, E.E., Petitgirard, S., Delitz, J.T., Wendt, M., Bican, Y. and Ehnes, A. (2015). The extreme conditions beamline P02. 2 and the extreme conditions science infrastructure at PETRA III. Journal of synchrotron radiation, 22(4), pp.908-924.

Lobanov, S.S., Dong, X., Martirosyan, N.S., Samtsevich, A.I., Stevanovic, V., Gavryushkin, P.N., Litasov, K.D., Greenberg, E., Prakapenka, V.B., Oganov, A.R., and Goncharov, A.F. (2017). Raman spectroscopy and X-ray diffraction of sp^3-$CaCO_3$ at lower mantle pressures. Physical Review B, 96, 104101

Lobanov, S.S., Schifferle, L., and Schulz, R. (2020). Gated detection of supercontinuum pulses enables optical probing of solid and molten silicates at extreme pressure–temperature conditions. Review of Scientific Instruments, 91, 053103.

Martirosyan, Naira S., Ilias Efthimiopoulos, Lea Pennacchioni, Richard Wirth, Sandro Jahn, and Monika Koch-Müller. (2021). Effect of cationic substitution on the pressure-induced phase transitions in calcium carbonate. American Mineralogist: Journal of Earth and Planetary Materials 106(4), 549-558.

Mao, Z., Armentrout, M., Rainey, E., Manning, C.E., Dera, P., Prakapenka, V.B., and Kavner, A. (2011). Dolomite III: A new candidate lower mantle carbonate. Geophysical Research Letters, 38(22), L22303.

Merlini, M., Cerantola, V., Gatta, G.D., Gemmi, M., Hanfland, M., Kupenko, I., Lotti, P., Müller, H., and Zhang, L. (2017). Dolomite-IV: Candidate structure for a carbonate in the Earth's lower mantle. American Mineralogist, 102, 1763-1766.

Merlini, M., Crichton, W.A., Hanfland, M., Gemmi, M., Muller, H., Kupenko, I., and Dubrovinsky, L. (2012). Structures of dolomite at ultrahigh pressure and their influence on the deep carbon cycle. The Proceedings of the National Academy of Sciences, 109, 13509-14.

Ovsyannikov, S.V., Shchennikov, V.V., Shvetsova, M.A., Dubrovinsky, L.S., and Polian, A. (2010). Tuning of the stoichiometry of $Fe_{1-x}O$ wüstite by compression. Physical Review B, 81, 060101.

Plank, T., and Manning, C.E. (2019). Subducting carbon. Nature, 574, 343-352.

Prescher, C., and Prakapenka, V.B. (2015). DIOPTAS: a program for reduction of two-dimensional X-ray diffraction data and data exploration. High Pressure Research, 35, 223-230.

Reeder, R.J., and Dollase, W.A. (1989). Structural variation in the dolomite-ankerite solid-solution series; an X-ray, Moessbauer, and TEM study. American Mineralogist, 74, 1159-1167.

Rividi, N., van Zuilen, M., Philippot, P., Menez, B., Godard, G., and Poidatz, E. (2010). Calibration of carbonate composition using micro-Raman analysis: application to planetary surface exploration. Astrobiology, 10, 293-309.

Shen, G., Wang, Y., Dewaele, A., Wu, C., Fratanduono, D.E., Eggert, J., Klotz, S., Dziubek, K.F., Loubeyre, P., and Fat'yanov, O.V. (2020). Toward an international practical pressure scale: A proposal for an IPPS ruby gauge (IPPS-Ruby2020). High Pressure Research, 40, 299-314.

Shirasaka, M., Takahashi, E., Nishihara, Y., Matsukage, K., and Kikegawa, T. (2002). In situ X-ray observation of the reaction dolomite= aragonite+ magnesite at 900–1300 K. American Mineralogist, 87, 922-930.

Sleep, N.H., and Zahnle, K. (2001). Carbon dioxide cycling and implications for climate on ancient Earth. Journal of Geophysical Research: Planets, 106, 1373-1399.

Stachel, T., Harris, J.W., and Brey, G.P. (1998). Rare and unusual mineral inclusions in diamonds from Mwadui, Tanzania. Contributions to Mineralogy and Petrology, 132, 34-47.

Stachel, T., Harris, J.W., Brey, G.P., and Joswig, W. (2000). Kankan diamonds (Guinea) II: lower mantle inclusion parageneses. Contributions to Mineralogy and Petrology, 140, 16-27.

Toby, B.H. (2001). EXPGUI, a graphical user interface for GSAS. Journal of Applied Crystallography, 34, 210-213.

Vennari, C.E., and Williams, Q. (2018). A novel carbon bonding environment in deep mantle high-pressure dolomite. American Mineralogist, 103, 171-174.

Walter, M.J., Bulanova, G.P., Armstrong, L.S., Keshav, S., Blundy, J.D., Gudfinnsson, G., Lord, O.T., Lennie, A.R., Clark, S.M., Smith, C.B., and Gobbo, L. (2008). Primary carbonatite melt from deeply subducted oceanic crust. Nature, 454, 622-630.

White, W. (1974). The carbonate minerals: In the Infrared spectra of minerals (Edited by VC Farmer). Mineralogical Society, London.

Wirth, R. (2009). Focused Ion Beam (FIB) combined with SEM and TEM: Advanced analytical tools for studies of chemical composition, microstructure and crystal structure in geomaterials on a nanometre scale. Chemical Geology, 261, 217-229.

Wirth, R., Kaminsky, F., Matsyuk, S., and Schreiber, A. (2009). Unusual micro- and nano-inclusions in diamonds from the Juina Area, Brazil. Earth and Planetary Science Letters, 286, 292-303.

Wojdyr, M. (2010). Fityk: a general-purpose peak fitting program. Journal of Applied Crystallography, 43, 1126-1128.

Zhao, C., Xu, L., Gui, W., and Liu, J. (2020). Phase stability and vibrational properties of iron-bearing carbonates at high pressure. Minerals, 10, 1142.

Figure captions

Fig. 1. Experimental conditions and high-pressure phases of ferroan dolomite with different iron content. Experiments with Ne pressure medium (PM) are marked by circles and diamonds. Diamonds represent pressure points at which Raman spectra were measured; circles – powder XRD. Experiments with Ar and NaCl PM are marked by triangles. Colors indicate phases detected at each experimental point: red, rose and orange – Dol-I; green and yellow – Dol-II; blue and purple – Dol-IIIc/IIIb. Grey lines are linear fits of the observed phase transition pressures as a function of *xFe*.

Fig. 2. Raman shifts of the dolomite bands with increasing iron content at atmospheric pressure. Red diamonds are related to the ν_1 symmetric stretching vibration of the CO_3 groups; the purple circles-ν_4; the blue triangles and green circles are related to the lattice vibration modes.

Fig. 3. Raman spectra of Ank40 collected at pressures up to 22.6 GPa showing the transition from Dol-I to Dol-II. The spectra have been normalized with respect to the highest value of each frequency region in order to facilitate direct comparison, whereas the background has been subtracted. Spectra are offset vertically for clarity. The same applies for Fig. 4-6 and to Fig. 8a.

Fig. 4. Raman spectra of Ank40 showing Dol-II to Dol-IIIb transition.

Fig. 5. Evolution of the stretching vibration modes in Ank64 upon compression up to 43.7 GPa. The dotted lines show a shift of the Raman bands caused likely by the spin transition.

Fig. 6. Raman spectra at ~40 GPa in the high-frequency range. a-d) experimental spectra; e) spectrum of Fe-poor dolomite from (Efthimiopoulos et al 2019).

Fig. 7. The Rietveld refinement of the Ank40 (a) and Ank23 (b) XRD patterns, using Dol-IIIb (wR = 19.9%) and Dol-IIIc (wR = 18.5%) models in combination with Ne. The

experimental curve is indicated with crosses. The green and blue lines represent the calculated XRD and the difference curve. The Bragg positions of Dol-IIIb or IIIc (in black) and Ne (in blue) are marked by ticks.

Fig. 8. Results of the Raman spectroscopy (a) and TEM (b,c) analyses of the Ank23 sample recovered after heating above 2600 K at 43GPa. Sample was analyzed in the heated spot (top spectrum) and in the not heated area (bottom). While not heated area shows presence of the initial ferrous dolomite with Dol-I structure, in the heated area a mixture of phases (CC-I – calcite, Fe-oxide) could be recognized. B, c) TEM analyses show the presence of amorphous ferrous dolomite (Dol) and calcite.

Table 1. Composition of the dolomite-ankerite solid solutions (wt%) measured by microprobe analyses.

Sample	Formula	MgO	FeO	CaO	MnO	Total
				wt. %		
Ank19	$Ca(Mg_{0.81}Fe_{0.19})(CO_3)_2$	17.2 (0.5)	7.1 (0.5)	29.6 (0.6)	0.03 (0.02)	53.93
Ank23	$Ca_{0.97}(Mg_{0.77}Fe_{0.23}Mn_{0.03})(CO_3)_2$	16.6 (0.9)	9 (1)	29.0 (0.3)	1.1 (0.1)	55.70
Ank40	$Ca_{0.99}(Mg_{0.55}Fe_{0.40}Mn_{0.06})(CO_3)_2$	11.3 (0.4)	14.7 (0.4)	28.2 (0.3)	2.2 (0.2)	56.4
Ank64	$Ca_{0.99}(Mg_{0.33}Fe_{0.64}Mn_{0.05})(CO_3)_2$	6 (2)	22 (2)	26.9 (0.5)	1.7 (0.1)	56.6
Standards	Dolomite	22.20	0.11	30.53	0.04	52.88
	Calcite	-	0.04	54.84	0.11	54.99
	Siderite	0.12	59.06	-	2.80	61.98

Notes: Average compositions and standard deviations (in brackets) are given based on 6-12 measurements for each phase.

Table 2. Unit cell parameters of the Dol-III/IIIb high-pressure modifications.

P (GPa)	Sample	Formula	Phase	Unit cell *a*, *b*, *c* (Å); *α*, *β*, *γ* (°); *V* (Å^3)
44	Ank23	$Ca_{0.97}(Mg_{0.77}Fe_{0.23}Mn_{0.03})(CO_3)_2$	Dol-IIIc (SG $P\bar{1}$, *Z*= 8)	4.544(1), 11.172(5), 13.715 (5); 69.9(9), 88.4(6), 89.4(8); 653.9(5)
41	Ank40	$Ca_{0.99}(Mg_{0.55}Fe_{0.40}Mn_{0.06})(CO_3)_2$	Dol-IIIb (SG *R*3, *Z*= 21)	11.905(5), 11.905(5), 13.646(8); 90, 90, 120; 1674.9(2)
38	Ank64	$Ca_{0.99}(Mg_{0.33}Fe_{0.64}Mn_{0.05})\ (CO_3)_2$	Dol-IIIb (SG *R*3, *Z*= 21)	11.969(5), 11.969(5), 13.659(8); 90, 90, 120; 1694.6(2)
39	Merlini et al 2012	$Ca(Mg_{0.6}Fe_{0.4})(CO_3)_2$	Dol-IIIb (SG *R*3, *Z*= 21)	11.97(9), 11.97(9), 13.66(12); 90, 90, 120; 1674.9(2)
43	Binck et al 2020	$Ca(Mg_{0.98}Fe_{0.02})\ (CO_3)_2$	Dol-IIIc (SG $P\bar{1}$, *Z*= 8)	4.452(4), 11.168(17), 13.696(17); 69.0, 88.3, 89.3; 635.64

Note: Ank19 was not studied by XRD, as the latter exhibits an almost identical Raman spectroscopic behavior to Ank23 under high pressure

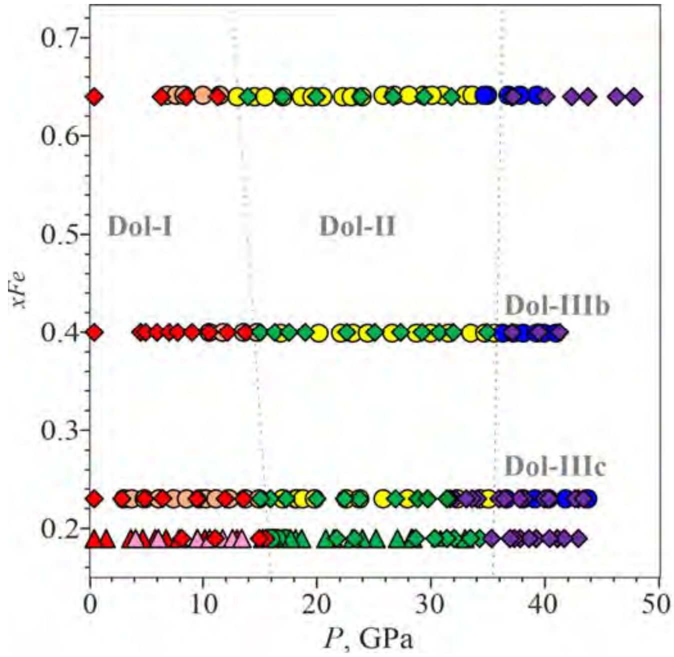

Fig. 1. Experimental conditions and high-pressure phases of ferroan dolomite with different iron content. Experiments with Ne pressure medium (PM) are marked by circles and diamonds. Diamonds represent pressure points at which Raman spectra were measured; circles – powder XRD. Experiments with Ar and NaCl PM are marked by triangles. Colors indicate phases detected at each experimental point: red, rose and orange – Dol-I; green and yellow – Dol-II; blue and purple – Dol-IIIc/IIIb. Grey lines are linear fits of the observed phase transition pressures as a function of *xFe*.

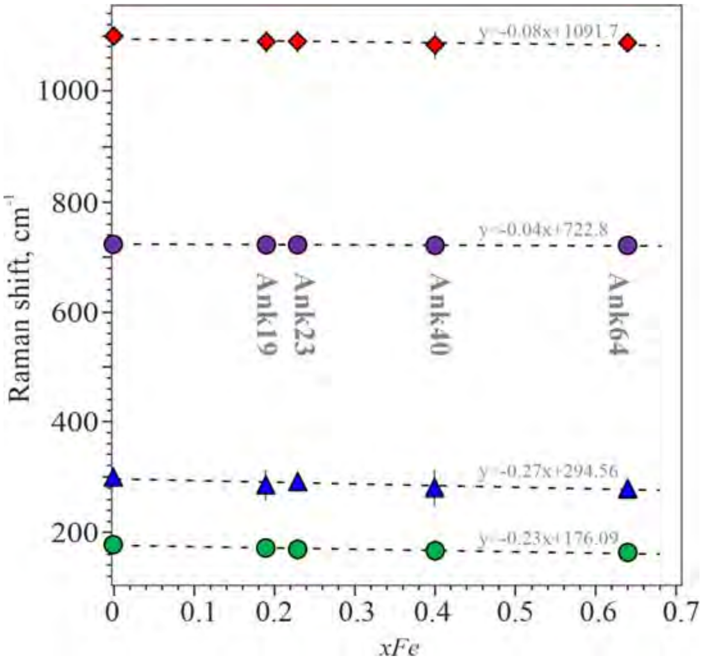

Fig. 2. Raman shifts of the dolomite bands with increasing iron content at atmospheric pressure. Red diamonds are related to the ν_1 symmetric stretching vibration of the CO_3 groups; the purple circles-ν_4; the blue triangles and green circles are related to the lattice vibration modes.

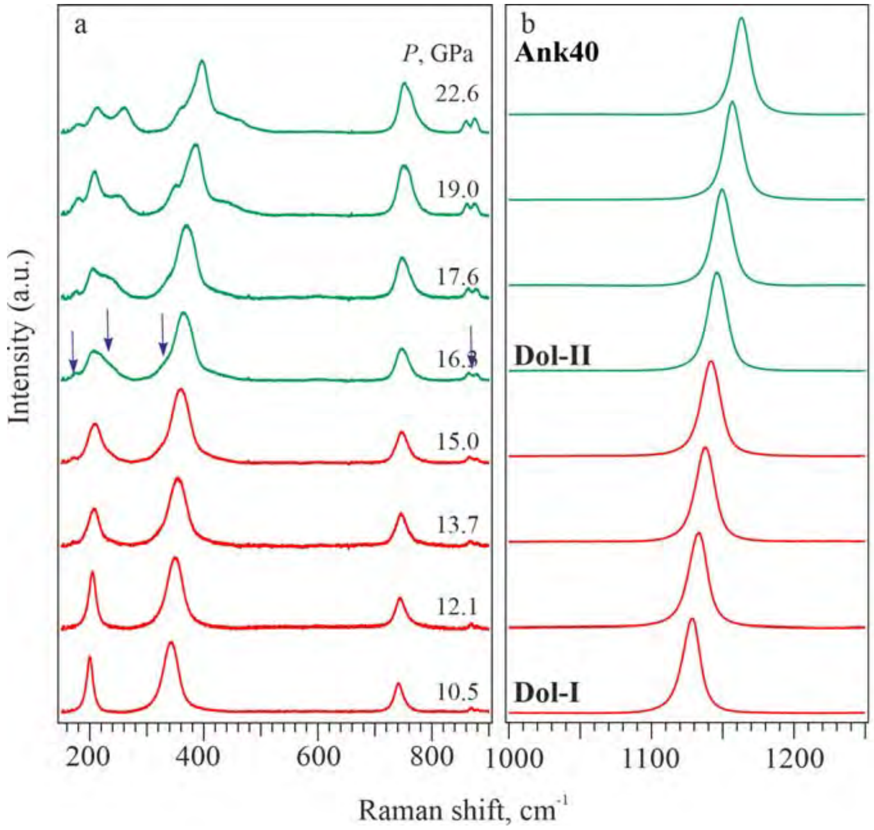

Fig. 3. Raman spectra of Ank40 collected at pressures up to 22.6 GPa showing the transition from Dol-I to Dol-II. The spectra have been normalized with respect to the highest value of each frequency region in order to facilitate direct comparison, whereas the background has been subtracted. Spectra are offset vertically for clarity. The same applies for Fig. 4-6 and to Fig. 8a.

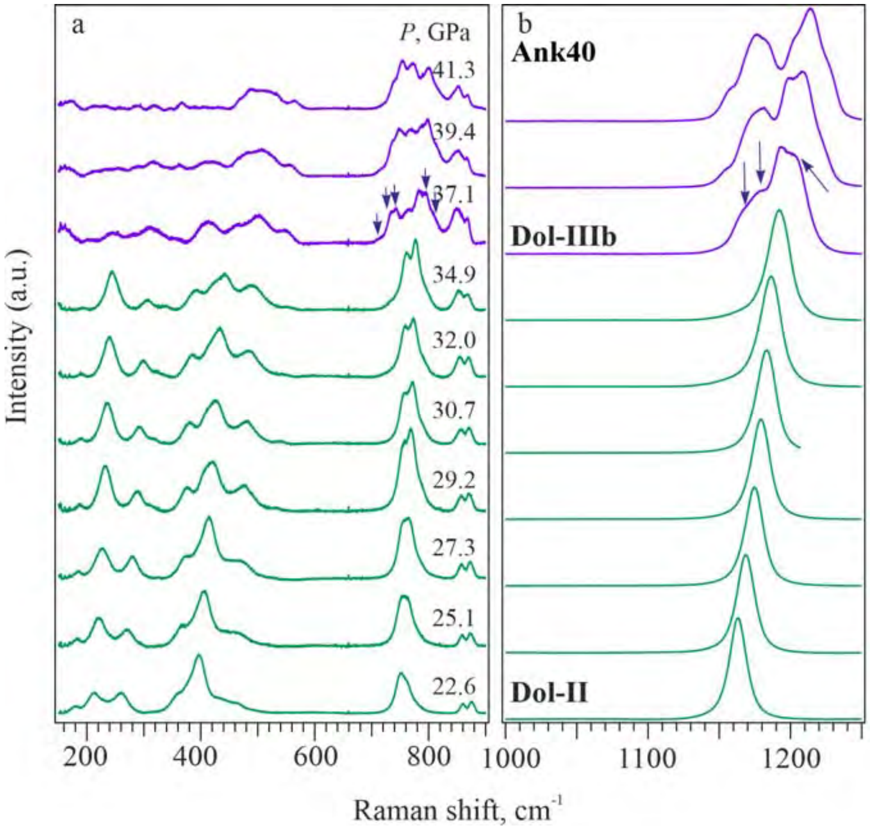

Fig. 4. Raman spectra of Ank40 showing Dol-II to Dol-IIIb transition.

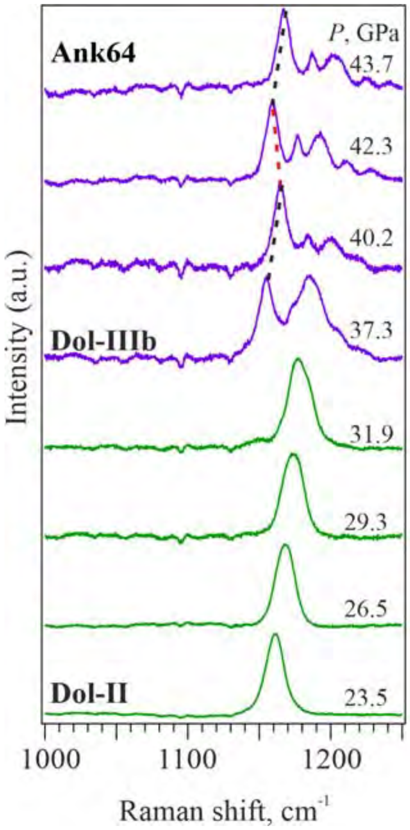

Fig. 5. Evolution of the stretching vibration modes in Ank64 upon compression up to 43.7 GPa. The dotted lines show a shift of the Raman bands caused likely by the spin transition.

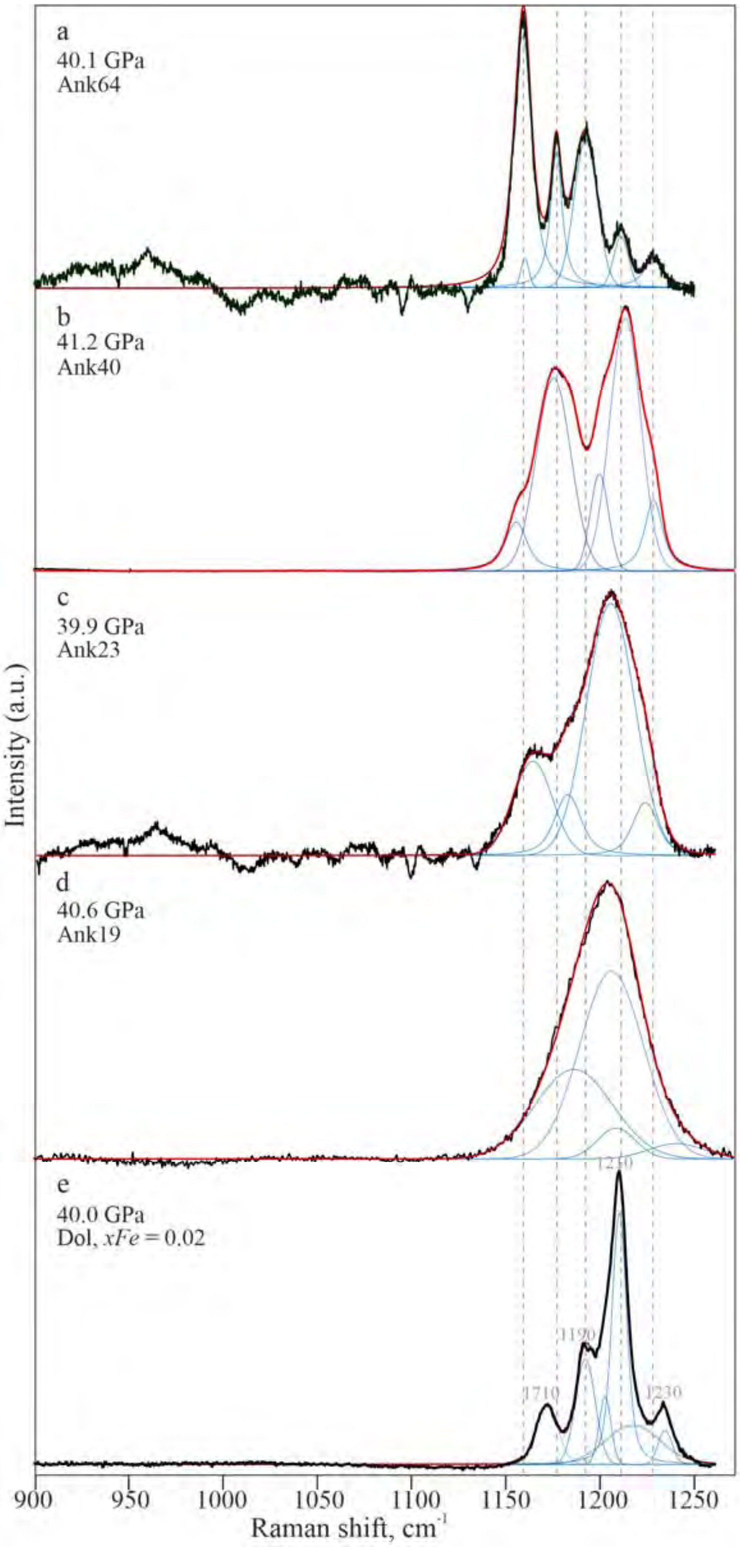

Fig. 6. Raman spectra at ~40 GPa in the high-frequency range. a-d) experimental spectra; e) spectrum of Fe-poor dolomite from (Efthimiopoulos et al 2019).

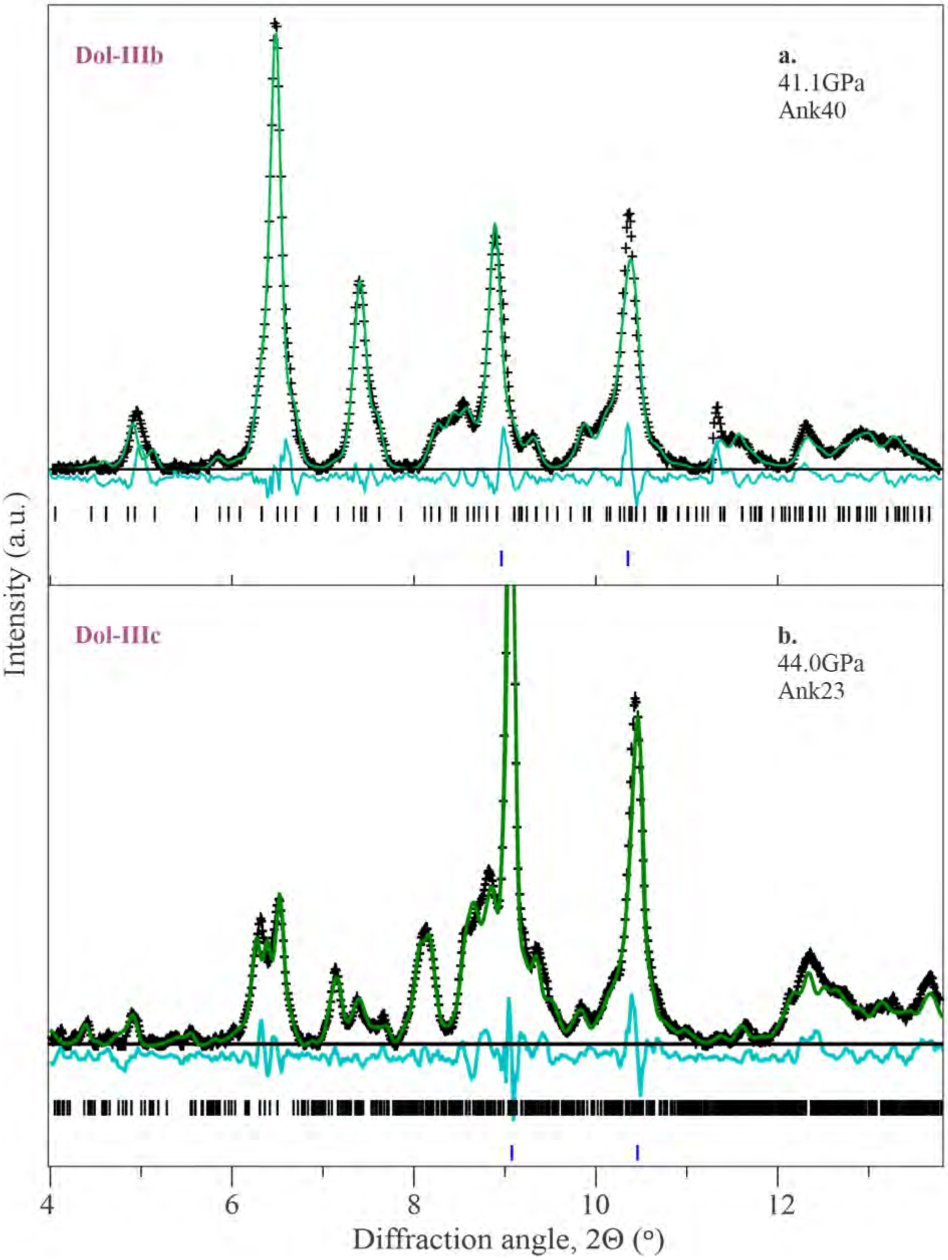

Fig. 7. The Rietveld refinement of the Ank40 (a) and Ank23 (b) XRD patterns, using Dol-IIIb (wR = 19.9%) and Dol-IIIc (wR = 18.5%) models in combination with Ne. The experimental curve is indicated with crosses. The green and blue lines represent the calculated XRD and the difference curve. The Bragg positions of Dol-IIIb or IIIc (in black) and Ne (in blue) are marked by ticks.

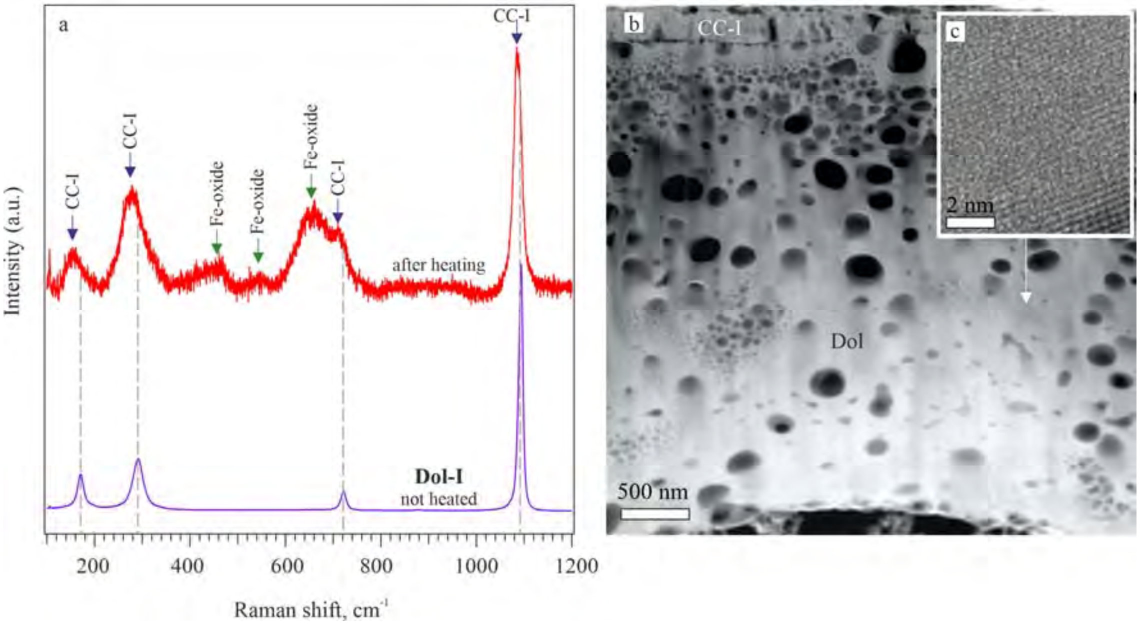

Fig. 8. Results of the Raman spectroscopy (a) and TEM (b,c) analyses of the Ank23 sample recovered after heating above 2600 K at 43GPa. Sample was analyzed in the heated spot (top spectrum) and in the not heated area (bottom). While not heated area shows presence of the initial ferrous dolomite with Dol-I structure, in the heated area a mixture of phases (CC-I – calcite, Fe-oxide) could be recognized. B, c) TEM analyses show the presence of amorphous ferrous dolomite (Dol) and calcite.